PCCP

Quantum simulations of thermally activated delayed fluorescence in an all-organic emitter

SCHOLARONE™
Manuscripts

Quantum simulations of thermally activated delayed fluorescence in an all-organic emitter

Tommaso Francese[1], Arpan Kundu[1], Francois Gygi[2] and Giulia Galli[1,3,4*]

[1]Pritzker School of Molecular Engineering, University of Chicago, Chicago, IL 60637, USA

[2]Department of Computer Science, University of California, Davis, CA 95616, USA

[3]Materials Science Division and Center for Molecular Engineering, Argonne National Laboratory, Lemont, IL 60439, USA

[4]Department of Chemistry, University of Chicago, Chicago, IL 60637, USA

KEYWORDS: TADF, DFT, FPMD, Nuclear Quantum Effects, NAI-DMAC

ABSTRACT

We investigate the prototypical NAI-DMAC thermally activated delayed fluorescence (TADF) emitter in the gas phase- and high-packing fraction limits at finite temperature, by combining first principles molecular dynamics with a quantum thermostat to account for nuclear quantum effects (NQE). We find a weak dependence of the singlet-triplet energy gap (ΔE_{ST}) on temperature in both the solid and the molecule, and a substantial effect of packing. While the ΔE_{ST} vanishes in the perfect crystal, it is of the order of ~ 0.3 eV in the molecule, with fluctuations ranging from 0.1 to 0.4 eV at 300 K. The transition probability between HOMO and LUMO molecular orbitals has a stronger dependence on temperature than the singlet-triplet gap, with a desirable effect for thermally activated fluorescence; such temperature effect is weaker in the condensed phase than in the molecule. Our results on ΔE_{ST} and oscillator strengths, together with our estimates of direct and reverse intersystem crossing rates, show that optimization of packing and geometrical conformation is critical to increase the efficiency of TADF compounds. Our findings highlight

the importance of considering thermal fluctuations and NQE to obtain robust predictions of the electronic properties of NAI-DMAC.

INTRODUCTION

Organic light-emitting diodes (OLEDs) are light sources used for a variety of applications, including displays and lighting[1], and they have been realized based on three generations of molecular emitters, relying on fluorescence (first generation), phosphorescence (second generation), and thermally activated delayed fluorescence (TADF, third generation) processes (see Fig.1). Fluorescent OLEDs use organic dyes where only the transition of singlet excitons to the singlet ground state ($S_1 \rightarrow S_0$) is allowed, and thus about 25% of the excitons are typically harvested for luminescence. Hence the external quantum efficiency (EQE) of fluorescent OLEDs is rather low, below 5%. Phosphorescent OLEDs use molecular complexes containing heavy metals (*e.g.*, Iridium or Platinum) to enable spin-orbit coupling between the lowest lying singlet (S_1) and triplet (T_1) excited states. Such coupling can accelerate the radiative deactivation from T_1 to S_0 and facilitate inter-system-crossing (ISC) from S_1 to T_1. The strategy adopted in the second-generation OLEDs has led to a considerable increase of the emission efficiency but also to environmental and cost concerns due to the utilization of rare heavy metals. One solution has been proposed in the pioneering work of Adachi[2], using all organic TADF[3] molecules without heavy metals, thus paving the way to the third generation of OLEDs. TADF molecules usually exhibit a small energy gap of few meV (ΔE_{ST}) between S_1 and T_1. If the lifetime of the T_1 excitons is sufficiently long, the reverse intersystem crossing (*r*ISC) process, spin-forbidden at T=0 K, may be thermally activated; hence the triplet excitons can up-convert into the S_1 state from which they radiatively relax to the ground state, leading to a theoretical internal QE of 100%. The triplet state T_1 effectively acts as an exciton "reservoir", hosting 75% of the excitons generated by

injections of holes (h^+) and electrons (e^-) carriers into the OLED organic molecule. Some TADF compounds have shown[4, 5] up to 38% external QE.
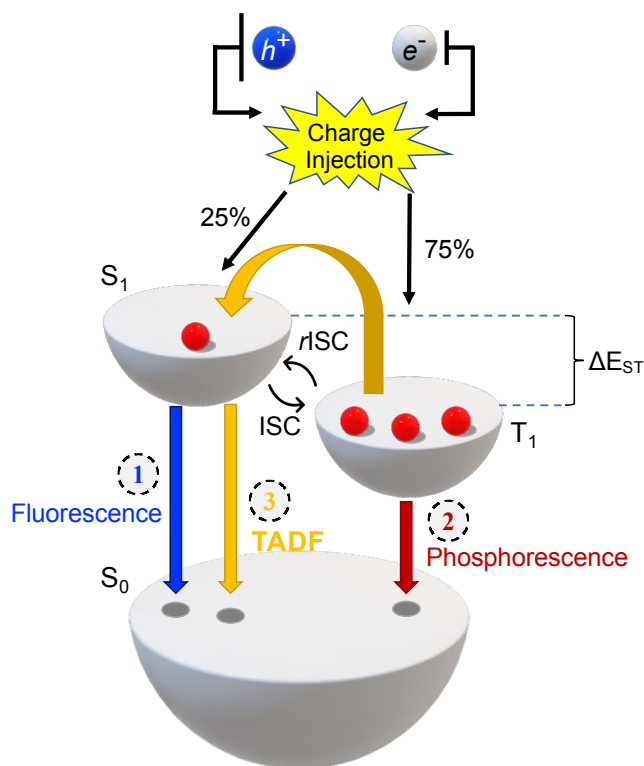

Figure 1. *Schematic representation of OLED technologies.* (1) Fluorescence (blue), (2) Phosphorescence (red) *via* intersystem crossing (ISC) and (3) Thermally Activated Delayed Fluorescence (TADF) (yellow) via reverse intersystem crossing (rISC). The excitons generated by holes and electrons recombination are formed in a 1:3 ratio in the singlet (S_1) and triplet (T_1) excited states, respectively, separated by the energy ΔE_{ST}. S_0 is the ground state.

Unfortunately, the potential use of TADF-OLEDs is still hindered by the intrinsic difficulty of precisely controlling the harvesting of excitons and avoiding the non-radiative recombination processes in the T_1 level, which may lead to the conversion of excitons into heat. The realization of a functioning rISC mechanism requires a delicate balance between two conflicting requirements: a small S_1/T_1 energy splitting (a value $\Delta E_{ST} < 0.37$ eV has been suggested by Yersin[6]) and a high radiative rate constant ($>10^6$ s^{-1}), in addition to favorable direct and reverse intersystem crossing rates. To meet the requirements several TADF

molecules have been explored, with different donor (D) - acceptor (A) linking architectures[7-13]. Although robust structural descriptors have not yet been identified, it has been suggested[14] that the nature of the donor and acceptor moieties should be carefully chosen so as to obtain a torsional angle ($\theta°$) between them that minimizes the overlap between the highest occupied molecular orbitals (HOMO) and lowest unoccupied molecular orbitals (LUMO) of the TADF compound.

Here we focus on a prototypical and promising TADF compound, NAI-DMAC[15], and present insights into the optimal conditions of operation based on first principles calculations. NAI-DMAC is one of the few orange-red emitters[16-20] reported in the literature with high EQE (>23%), and displays a relatively simple D-A conformation (see Fig.2). The NAI-DMAC molecule has also been recently used as a basic unit to create a polymer[21], expanding its potential application for medical purposes as a contrast emitter. Experimentally, the S_1 and T_1 energy levels of NAI-DMAC have been determined via fluorescence (T=300 K) and phosphorescence (T=77 K) measurements[22, 23], and the TADF nature of the system has been confirmed[6] through transient photoluminescence of prompt (PT) and delayed (DL) fluorescence. Spectroscopic measurements have been performed both in solution (*i.e.*, toluene) and by employing the host matrix (mCPCN)[24]. The observed change in photoluminescence as a function of the NAI-DMAC concentration has been attributed to a variation in the molecule rigidity, or in the geometrical conformation induced by the matrix.

From a theoretical standpoint, although the properties of the isolated molecule at T=0 K have been investigated using calculations based on TDDFT[25, 26], no theoretical investigation has so far been reported of the NAI-DMAC crystal or of molecular aggregates in condensed phases. Thus, a mechanistic understanding of how the properties of NAI-DMAC vary from the gas to the condensed phase is not yet
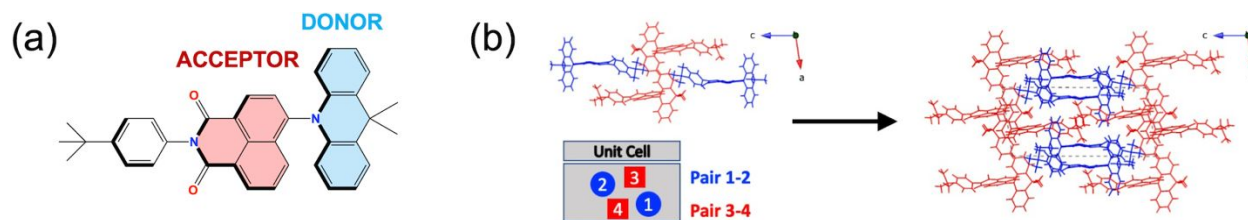
available.

Figure 2. *Schematic representation of the NAI-DMAC (C_{37}H_{32}N_2O_2) compound in the gas phase and solid state.* In (a) the NAI-molecule is shown, with the acceptor in red, and the DMAC-donor in blue. In (b) we show the four molecules in the crystal unit cell which are separated into two pairs (shown in red and blue, respectively). The molecules in each pair have similar geometrical conformations (see text).

However condensed phases of other molecular TADF molecules have been investigated using either continuum models or quantum mechanics/molecular mechanics (QM/MM)[27] approaches. For example, Lingling et al.[28] have included screening effects in the description of four TADF Cu(I)-based complexes in the solid state, by using an effective dielectric constant within a polarizable continuum model (PCM)[29, 30] approximation. Similarly, the apolar and polar dielectric environments were included in the study of F1, PTZ-DBTO2 and ACRXTN systems, and their influence on the fundamental key parameters of TADF molecules considered by J.-M. Mewes[31]. Their studies pointed at the importance of environmental effects, with results consistent with experiment. T. Hu[32] and collaborators investigated the influence of molecular orientation and torsional disorder of DMAC-TRZ with respect to mCPCM and mCP host matrixes via classical MD simulation combined with DFT and TDDFT electronic structure calculations. We note that in the study of ΔE_{ST} and transition dipole moments from MD snapshoots, T. Hu and co-workers found that the B3LYP[33-35] functional provides similar results to those obtained by using the ω*B97Xd functional, where the "ω" parameter is optimized with a "gap-tuning", system-dependent procedure[36]. In addition, investigations of several other D-A molecules, *i.e.*, AI-Cz[37], PPZ-PXZ and mDPBPZ-PXZ[38], and a D-A-D

system, DMF-BP-DMAC[39], have been reported using a QM/MM method[27] and TDDFT to study excited state levels (S_1 and T_1). These studies showed that ΔE_{ST} increases in going from a single solvated molecule to a solid-state aggregate of molecules at T=0 K. However, several other authors[40-44] reported an opposite trend, namely a sizeable decrease of ΔE_{ST} from the solvated molecule in the gas phase to the condensed phase, for a series of D-A systems, *e.g.*, TXO-TPA[40], SBF-BP-DMAC[41], DBT-BZ-PXZ[42], FDBQPXZ[43], PFBP-n[44]. These conflicting results have been obtained with similar computational methodologies (*e.g.*, QM/MM approaches combined with DFT and TDDFT electronic structure calculations) for different, albeit similar, systems. We note that one of the reasons of this discrepancy might be related to the different descriptions of environmental effects[45].
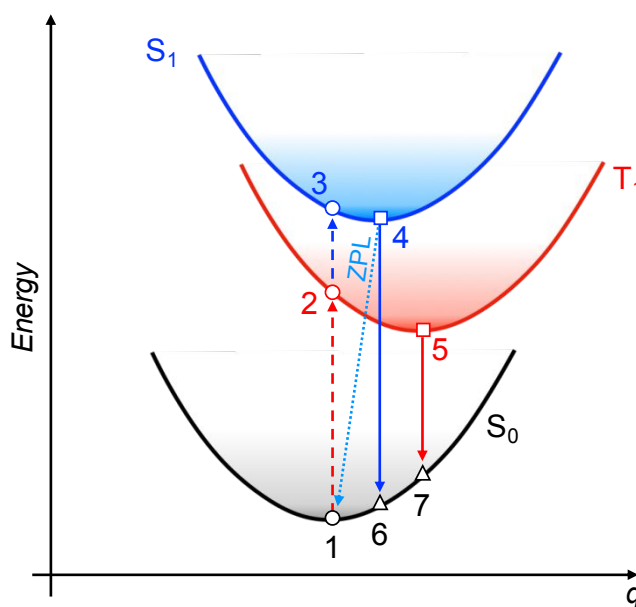

Figure 3. *Schematic representation of vertical and adiabatic processes investigated in this work.* At T=0, the vertical ΔE_{ST} energy difference is calculated as E(3)-E(2) and the adiabatic energy difference is computed as [E(4)- E(5)] (see text for the definition of vertical and adiabatic ΔE_{ST} at finite temperature). The zero-phonon line (ZPL) at T=0 K is given by E(4)-E(1).

Several levels of DFT and TDDFT theory have been adopted in the literature to describe the electronic properties of molecular TADF compounds (see *e.g.*, Bredas et al.[40]) and to interpret measured UV-vis absorption spectra[46-57], with calculations performed at zero temperature. Although TDDFT has been the method of choice in most cases, high level quantum chemistry techniques have also been adopted for some compounds, including Spin-Component Scaling second-order approximate Coupled-Cluster (SCS-CC2)[58, 59] or Density-Fitted second-order Quasidegenerate Perturbation theory[60] (DF-QDPT2). In addition to environmental effects, recent studies have focused on the vibrational contributions to TADF process, Wada[61] and co-workers investigated emission spectra, and S.W. Park[62] and collaborators studied fluorescence spectra.

Here we present a series of first principles calculations at zero and finite temperature aimed at understanding how conformation and temperature affect the ΔE_{ST} energy splitting and the electronic transition probability between ground and excited states of NAI-DMAC. We also present estimates of direct and reverse intersystem crossing rates. For the first time we carry out not only electronic structure calculations but also first principles MD (FPMD) at finite T and we include nuclear quantum effects (NQE) by coupling FPMD with a colored noise Langevin thermostat, or quantum thermostat[63]. Our results highlight the key role of thermal fluctuations and NQE in obtaining robust predictions of the electronic properties of NAI-DMAC. Furthermore, we analyze the difference between the structural and electronic properties of the system in the gas and solid state, showing the importance of packing and conformation in determining the excited state properties of this representative TADF compound.

RESULTS AND DISCUSSION

The geometry of the NAI-DMAC molecule in the gas phase and the unit cell of the solid are shown in

Figure 2. The system is composed of a N-(4-*tert*-butylphenyl)-1,8-naphthalimide (NAI) acceptor unit and

a 9,9-dimethyl-9,10-dihydroacridine (DMAC) donor unit; the NAI[64-66] moiety combines a highly rigid and

planar geometry together with a strong electron-withdrawing character. DMAC[67], on the other hand, has an

electron-donating character. In the following we report results on the energy difference between singlet and

triplet excited states (ΔE_{ST}, see Fig.3) and the transition probability between the lowest singlet excited state

and the ground state, which we simply characterized by the transition probability oscillator strength

(hereafter referred to as f_{OS}), given the low dielectric constant of the condensed system.

We first optimized the geometry of the molecule and of the solid at T=0 K, and we computed the energies

of the S_1 and T_1 states at the ground state equilibrium structures. We then optimized the geometries of the

singlet and triplet in the excited states using constrained DFT (see Fig. 1 and 3). To investigate finite T

properties, we carried out FPMD at T=300 K using both classical and quantum nuclear trajectories (see

Methods). We have recently shown that FPMD with a quantum thermostat accurately reproduces the

nuclear quantum effects on the electronic properties of a variety of carbon systems, by comparing QT results

to those of path-integral first principles MD simulations.[68]

From the equilibrated quantum (QTMD) and classical (FPMD) trajectories, we extracted sets of

uncorrelated configurations (see Method section) for which we computed the energies of S_1 and T_1 in both

the ground and excited state geometries. Our simulations were performed using the PBE[69, 70] functional, and

on PBE trajectories we computed both PBE and B3LYP excitation energies. We report below B3LYP

results, which for all the main, qualitative conclusions of this work agree with those of PBE calculations.

Following the notation of Fig. 3, we define vertical excitations at T=0 as the energy differences [E(3)-E(2)]; where E(3) and E(2) are computed at the geometry of E(1) (ground state geometry). During a QTMD or FPMD simulation we sample configurations around E(1), obtaining N values E^{gs} [I] with I=1,…N, where N=total number of configurations extracted from the MD simulations. The vertical energy difference between S_1 and T_1 (ΔE^V_{ST}) as a function of a MD run is computed as [E(3)- E(2)]$_I$; where E(3) and E(2) are computed at the geometry of E^{gs} [I]. Adiabatic energy differences (ΔE^A_{ST}) at T=0 K are computed as [E(4)-E(5)]; where E(4) and E(5) are evaluated at the geometry optimized in the S_1 and T_1 states, respectively. If the parabola defining the potential energy surfaces of S_0, S_1 and T_1 were parallel (that is if the equilibrium geometries of S_0, S_1 and T_1 coincided) then ΔE^A_{ST} would equal [E(4)$_I$- E(5)$_I$], where the energy of S_1 and T_1 are computed at the geometries "I" sampled during the MD for the ground state. However the S_0, S_1 and T_1 parabola are not parallel; we take into account, in an approximate way, how much the minima of the excited states are shifted relative to the minimum of the ground state by computing: ΔE^A_{ST} (I) = [E(4)$_I$-E(5)$_I$] + [E(7)-E^{gs}(I)] -[E(6)-E^{gs}(I)] where E(7) is computed at the equilibrium geometry of T_1 and E(6) is computed at the equilibrium geometry of S_1. By doing so we assume that the thermal contributions of the S_1 and T_1 states are approximately the same and hence cancel out. All total energies have been obtained with constrained DFT.

The transition probability between HOMO (H) and LUMO (L) states is proportional to $D^2_{HL} = |\langle \varphi_L | x | \varphi_H \rangle|^2$; in the case of the crystal, it is obtained using a method for periodic systems[71] implemented in the Qbox[72] code. The oscillator strength is defined as:

$$f_{OS} = \frac{2}{3} \cdot \frac{m_e}{\hbar^2 e^2} \cdot (e_L - e_H) \cdot D^2_{HL}$$

where m_e, $\hbar^2$ and e^2 are the mass of the electron, the reduced Planck constant and electron charge in atomic units, respectively. The $(e_L - e_H)$ is the energy difference between the single particle HOMO and LUMO singlet levels. Note that these oscillator strengths are only indicative of radiative processes as electron-phonon interaction is not included in the calculation of f_{OS}. However, as we discuss below the distribution of f_{OS} computed over MD trajectories provides an estimate of the effect of vibronic coupling on non-radiative processes.

Gas Phase Limit

At T=0 K, we find an equilibrium torsion angle of the molecule, $\theta = 84.2°$ similar to that reported experimentally[15], 83.7°, with HOMO and LUMO wavefunctions highly localized on the DMAC and NAI units (see Fig. 4a), respectively. In the optimized excited state structures the torsion angles are different from that of the ground state, $\theta = 80.9°$ for S_1 and $\theta = 75.3°$ for T_1 states. The corresponding electronic structure indicate that different excitation processes occur in the singlet and triplet states: charge-transfer (CT) for S_1 and localized excitation (LE) in T_1. Unfortunately, we could not directly compare with the optimized structures studied in the literature[15], since structural data were not reported. We found a HOMO-LUMO gap at the B3LYP level of theory, $E_{Gap} = 2.61$ eV, in good agreement with previous results, $E_{Gap} = 2.64$ eV[15].
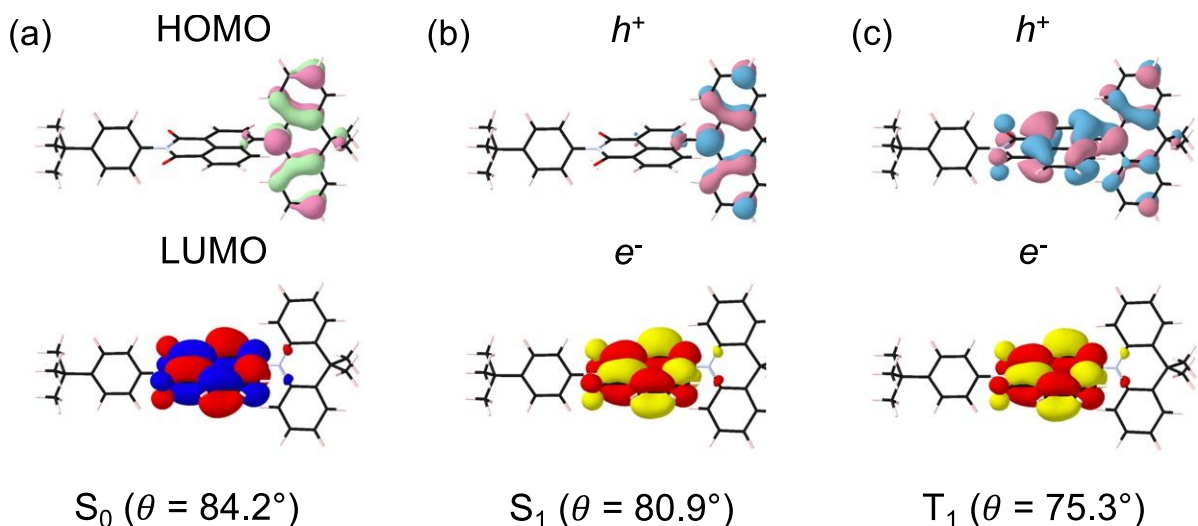
(a) HOMO (b) h^+ (c) h^+

LUMO e^- e^-

S_0 ($\theta = 84.2°$) S_1 ($\theta = 80.9°$) T_1 ($\theta = 75.3°$)

Figure 4. *Electronic structure of the optimized S_0, S_1 and T_1 configurations of the molecule NAI-DMAC.* (a) HOMO and LUMO levels in the S_0 state; (b) hole (h^+) and electron (e^-) localization in the S_1 state, yielding a charge transfer (CT) transition; (c) hole (h^+) and electron (e^-) localization in the T_1 state, yielding a LE transition.

Before proceeding with dynamical simulations, we investigate the dependence of the vertical energy difference ΔE^V_{ST} as a function of the torsion angle at T=0 K. We carried out a series of calculations for the isolated molecule by constraining the dihedral angle θ to a set of fixed values, as shown in Figure 5a. We found that ΔE^V_{ST} is minimum when the moieties D and A are orthogonal to each other. Note that the smallest value is obtained when the coordinates of the NAI and DMAC units are the same as in the ground state T=0 K structure (unrelaxed configuration in Figure 5a), indicating that the dihedral angle is a necessary albeit not sufficient geometrical parameter to determine the S_1/T_1 splitting. Unfortunately, the configuration where D and A are orthogonal to each other, while desirable to minimize ΔE^V_{ST}, yields an undesirable small value of f_{OS}, as shown in Figure 5b. We also estimated the reorganization energies of the singlet transition in the molecule as the difference between the vertical excitations (E[4]-E[1]) and the ZPL (see Fig.3) and we found that it is of the order of ~ 0.1 eV at the B3LYP level of theory.

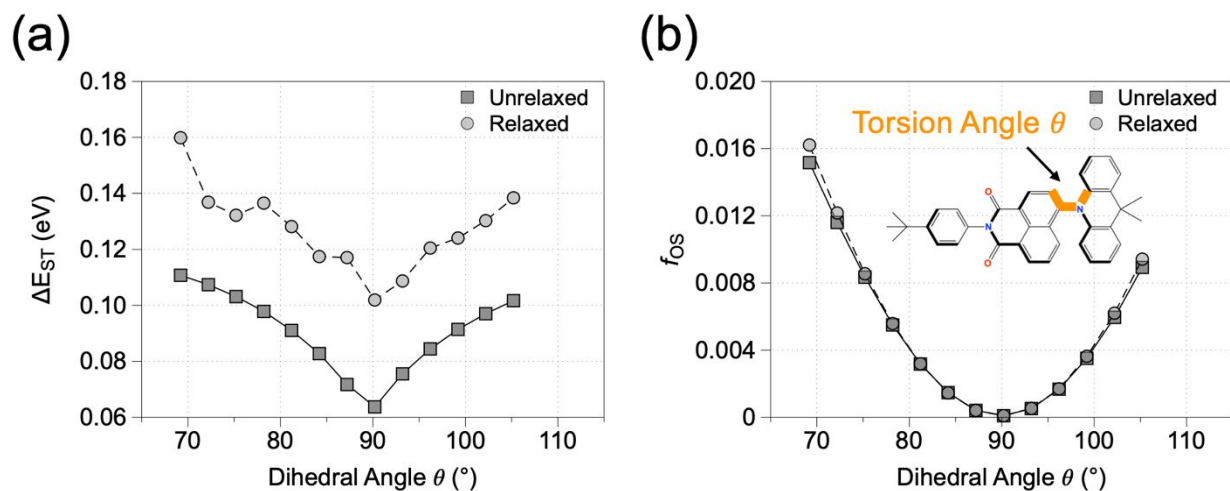**Figure 5.** *Electronic properties of NAI-DMAC in the gas phase as a function of the torsion angle θ.* (a) The vertical energy difference between triplet and singlet states (ΔE$_{ST}$), as a function of the molecular torsion angle (shown in the inset) between NAI and DMAC moieties for two sets of geometrical configurations: unrelaxed (only the torsion angle is varied) and relaxed (full geometrical optimization at each torsion angle value). (b) The oscillator strength f_{OS} (see text) as a function of the torsion angle. The values of this figure were obtained at the PBE level of theory.

We now turn to analyze the electronic structure of the molecule at finite T, to understand whether at 300 K the molecule may attain conformations for which both singlet-triplet splitting and the oscillator strength f_{OS} have desirable values.
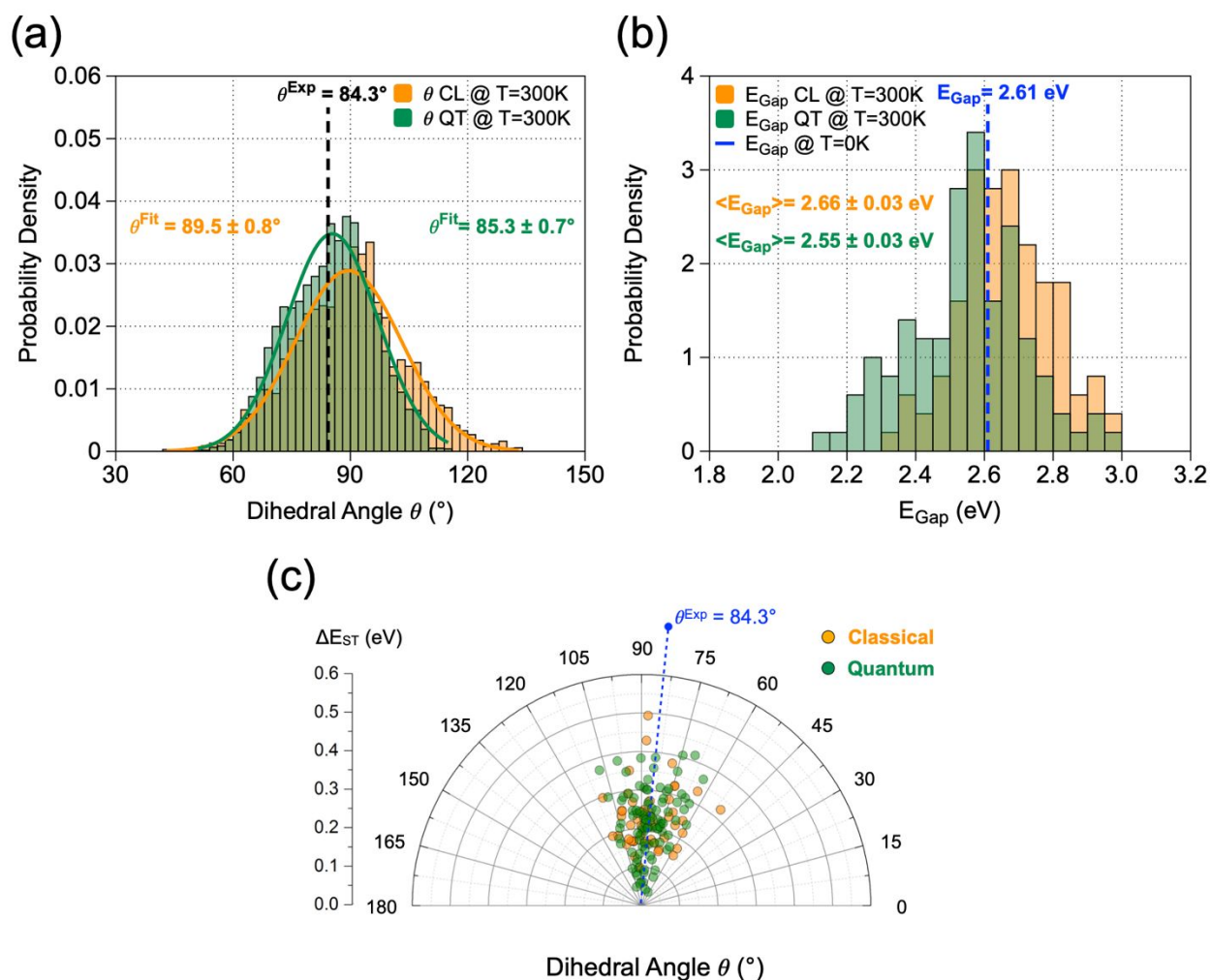
Figure 6. *Structural and electronic properties of the isolated molecule as a function of temperature.* (a) Probability distributions of the dihedral angle θ between NAI and DMAC moieties (see Fig. 5b) in the isolated molecule at 300K as obtained on classical (CL) and quantum (QT) trajectories (see text). The average values (θ^{fit}) of the distributions and the experimental (θ^{exp}) value are indicated. (b) Probability distributions of the HOMO-LUMO Gap (E_{Gap}) of the isolated molecule at 300K as obtained on classical (CL) and quantum (QT) trajectories. Averages values are indicated. (c) Values of the vertical singlet-triplet energy difference (ΔE_{ST}) as a function of θ for CL and QT trajectories.

Figure 6a shows the distributions of dihedral angles in the molecule at T=300 K, obtained with FPMD (classical nuclear trajectories, denoted as CL) and QTMD (quantum nuclear trajectories, denoted as QT). The two distributions cover a broad range of angles, with the average value of the quantum distribution

1

being about four degrees smaller than the classical one, and in closer agreement with experiments. Interestingly, at 300 K, the HOMO-LUMO gap of the molecule slightly increases relative to T=0 K in the case of classical trajectories but decreases when nuclear quantum effects are accounted for. The average values of ΔE_{ST} computed for the CL and QT distributions are instead the same, within error bars. The vertical energy differences slightly increase with temperature, but the approximate adiabatic values are basically the same at T=0 K and 300 K showing a weak dependence of the reorganization energy as a function of T (Fig. 7a and 7b).

The distribution of vertical ΔE_{ST} values as a function of the dihedral angle is shown in Figure 6c. As observed in the case of the molecule at T=0 K, we find that the value of the torsion angle is not a sufficient structural descriptor to predict the values of ΔE_{ST}. Indeed, we find rather different values of the singlet-triplet splitting for the same dihedral angle, depending on the overall configuration, both for CL and QT trajectories.
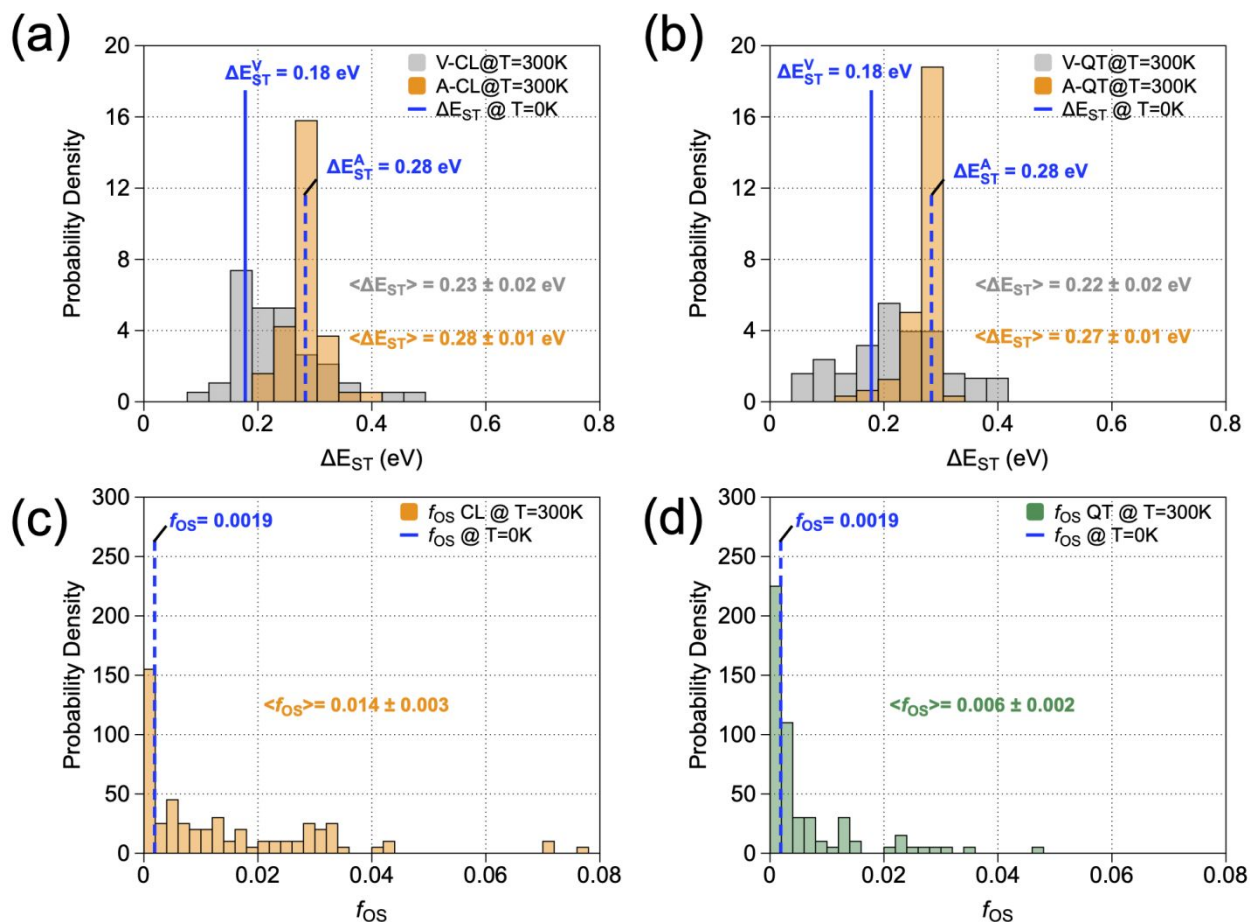
Figure 7. *Impact of nuclear quantum effects on the electronic properties of the molecule at finite temperature.* Probability distribution of the vertical (V) and adiabatic (A) singlet-triplet energy difference (ΔE_{ST}) at 300 K for classical (a) and quantum mechanical (b) trajectories. Probability distribution of the oscillator strength (f_{OS}) between HOMO and LUMO states of the molecule at 300 K computed on classical (c) and quantum (d) trajectories. The results shown in blue correspond to the values at T=0 K.

We have seen so far that while increasing the temperature leads to an increase of the vertical ΔE_{ST}, there is hardly any in the average adiabatic values relative to T=0 K. Interestingly, the temperature has a desirable effect on the oscillator strength which increases at 300 K, relative to T=0 K, by a factor of ~ 7 in the classical case and by a factor of ~ 3 when we include nuclear quantum effects. Hence our results show that in the

gas phase limit there is an overall desirable effect of the T on the electronic properties of NAI-DMAC. We

now turn to analyzing the properties of the solid, which is representative of the high-packing fraction limit.

High Packing Fraction Limit

There are four inequivalent molecules in the unit cell of the solid, that we have divided into pairs: P_{1-2} and

P_{3-4} (see Figure 2b). The torsion angles of molecules 1 and 2 are similar to the corresponding angle in the

gas phase, and different from those of molecules 3 and 4, which exhibit angles notably larger by more than

15 degrees. The optimized structure of the solid at T=0 K is in good agreement with that reported

experimentally ($\theta_{\#1}^{\text{X-ray}}$ = 84.3° vs $\theta_{\#1}^{\text{Opt}}$ = 85.7°, $\theta_{\#3}^{\text{X-ray}}$ = 97.4° vs $\theta_{\#3}^{\text{Opt}}$ = 99.3°). Figure 8 shows the

wavefunction corresponding to the electronic energy levels close to the valence band maximum and

conduction band minimum of the solid at T=0 K. The HOMO level is mostly localized on one of the

molecular pairs, but not entirely, suggesting that finite temperature fluctuations may give rise to *inter*-

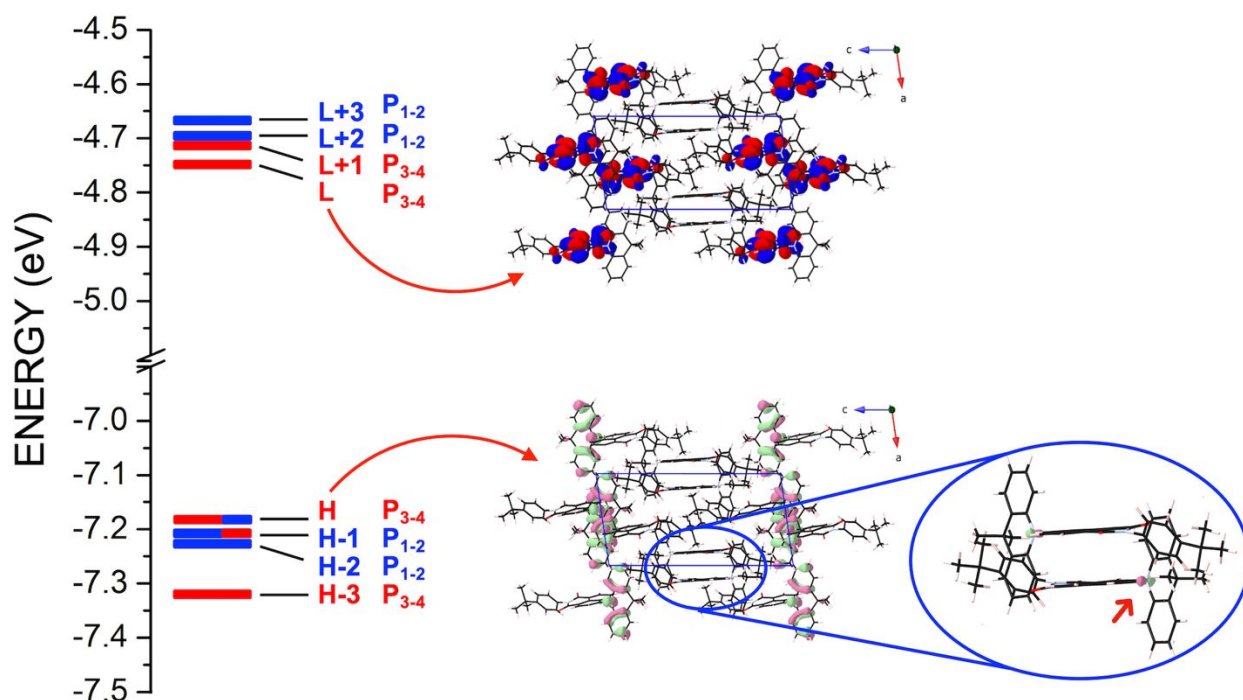molecular transitions between neighboring pairs, as discussed below.

Figure 8. *Schematic representation of the electronic structure of the solid at T=0 K.* Left - Electronic energy levels (computed using the B3LYP functional); the color of the levels depends on whether they are localized on blue or red pair of molecules. To the right of the graph are pictured iso-surfaces of the square-moduli of the HOMO and LUMO wavefunctions. The inset shows the partial localization of the wavefunction on the blue pair, suggesting the possibility of inter-molecular transitions.

Following the same computational protocol adopted for the isolated molecule, we carried out FPMD and QT-FPMD simulations of the solid at T=300 K at the PBE level of theory and we computed the electronic structure at the PBE and B3LYP level. Similar to the isolated molecule we found that the average angles of the QT distributions are slightly smaller than those of the CL ones and in overall better agreement with experiments (Fig. 9 a and b). As expected, the HOMO-LUMO gap (E_{Gap}) of the solid is smaller than that of the molecule (2.45 eV *vs* 2.61 eV at T=0 K, see Fig. 9 c and d) and as in the case of the molecule, it decreases with temperature and more so when nuclear quantum effects are included. Again, as expected, in the case of the crystal the vertical and adiabatic ΔE_{ST} are both close to zero, and interestingly with very small fluctuations induced by disorder at finite temperature. We note that for a perfect classical, periodic crystal at T=0 K, $\Delta E_{ST} = 0$ eV. However due to thermal fluctuations the perfect periodicity is broken and ΔE_{ST} may become different from zero. When quantum effects are included, due to zero-point motion ΔE_{ST} can be different from zero also at zero temperature. For the nuclear displacements due to zero-point motion and due to thermal fluctuations at finite T, we find that the variations of vertical and adiabatic ΔE_{ST} are within ~0.01 eV, hence much smaller than in the molecular case. Hence a high packing fraction is beneficial to minimize ΔE_{ST}. Unfortunately, the oscillator strength for the electronic transition, while close to that of the gas phase limit at T=0 K, shows a more moderate increase with temperature than in the molecular case: a factor of two for both classical and quantum trajectories (see Fig.10a and b). This difference with respect to the molecular case is due to the occurrence of *inter-molecular* transitions at finite temperature in the

solid, as shown in Figure 11 for classical trajectories. In Fig. 11 we show consecutive configurations extracted from a first principles MD trajectories (total length ~ 10 ps). For each of these configurations we marked the HOMO-LUMO transitions (vertical bars) and we indicated which orbitals are involved in the transition. The orbitals are marked as red or blue depending which type of molecule they are localized upon, following the color code adopted in Fig. 2. We find that in about 33% of the cases transitions occur between HOMO and LUMO states belonging to different molecules, and these are unfavorable transitions contributing to an overall decrease of the oscillator strength relative to the molecule. About 32 % (2.4%) of the transitions occur between HOMO and LUMO orbitals between molecules marked red (blue). Finally, about 32% of the transitions involve at least one orbital that is shared between different types of molecules. The important result shown here is that, by carrying out molecular dynamics simulations, we were able to observe temporal variations of the orbitals between which transitions occur and understand the effect of intra-molecular transitions in packed configurations such as those found in the solid phase.
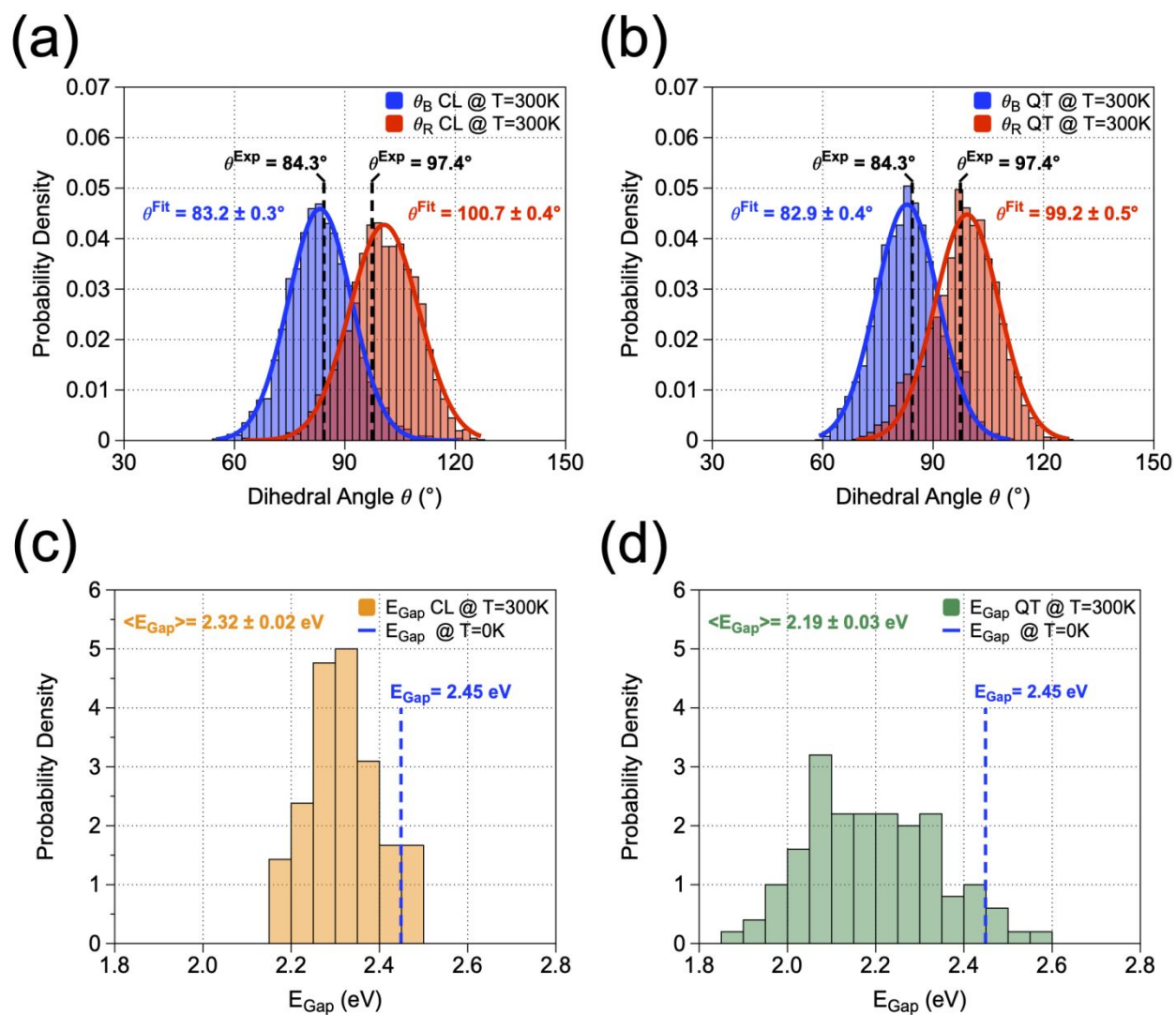
Figure 9. *Impact of nuclear quantum effects on the structure and energy gap of the solid at finite temperature.* Probability distribution of the torsion angles (θ) distributions at finite obtained on classical (a) and quantum (b) trajectories at 300 K. Probability distributions of the HOMO-LUMO obtained on classical (c) and quantum (d) trajectories. Results obtained at the B3LYP level of theory.
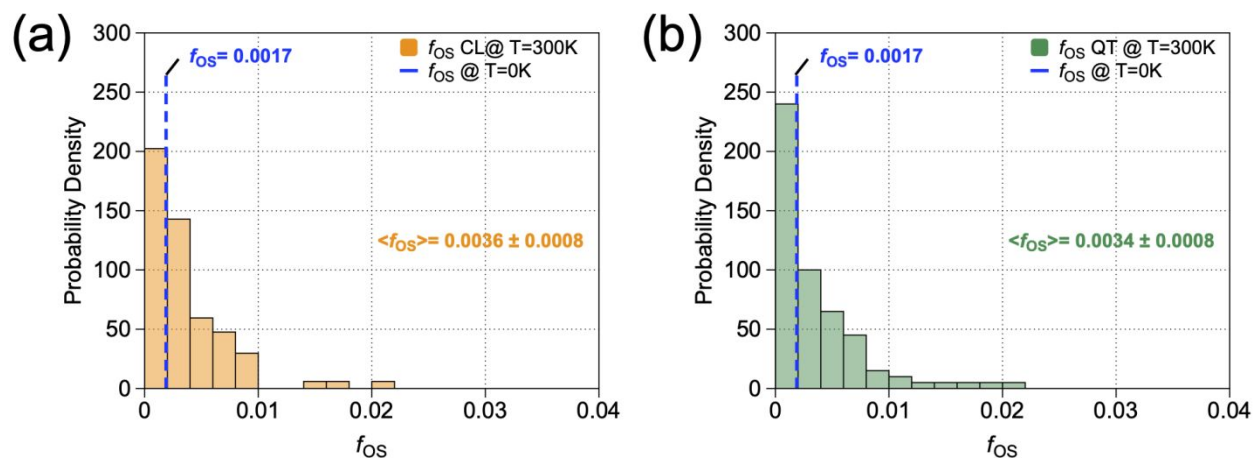
Figure 10. *Oscillator strength (f_{OS}) in the solid at finite temperature.* The f_{OS} distribution calculated for classical (a) and quantum (b) trajectories at 300 K.
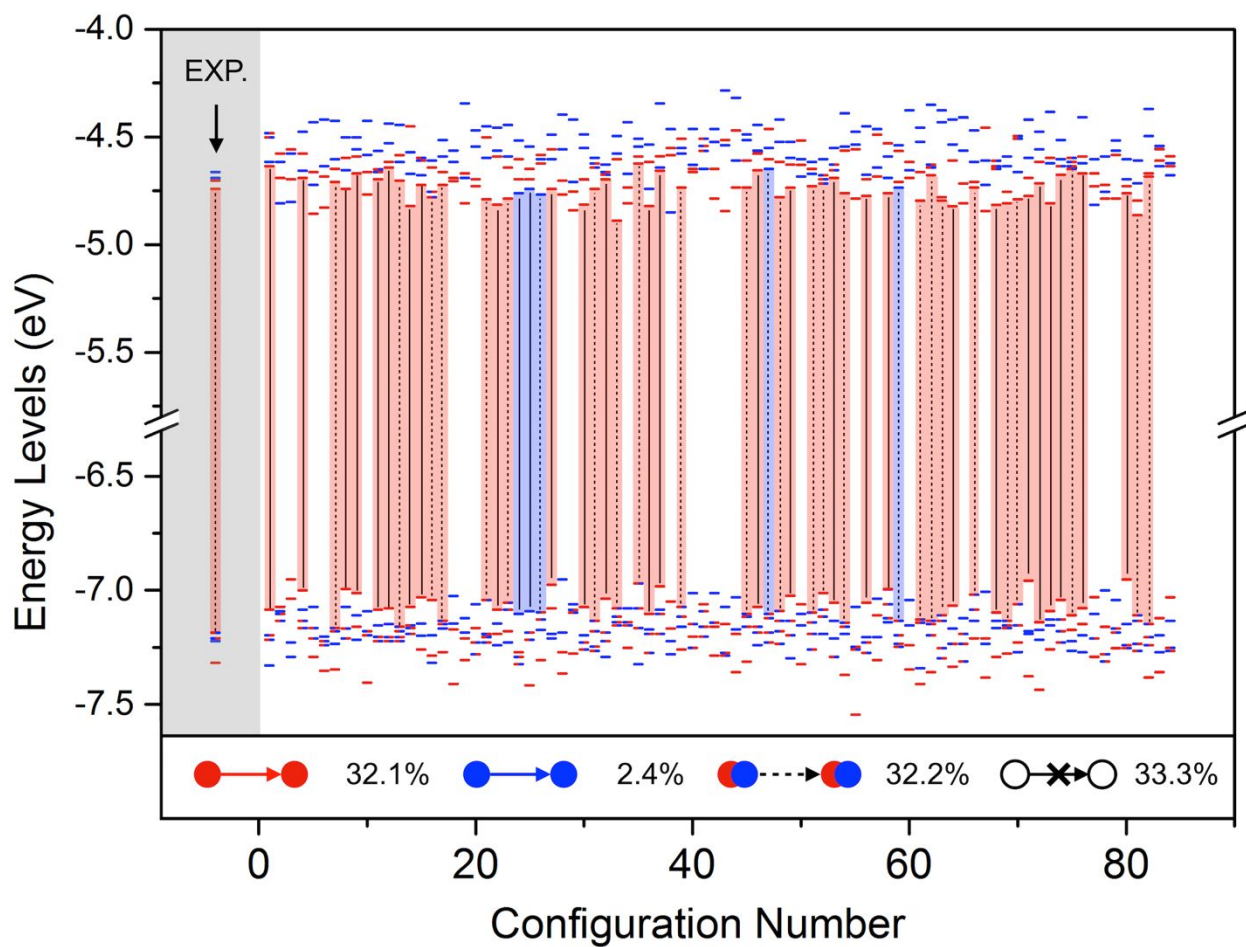
Figure 11. *Energy levels of the solid at finite temperature.* The HOMO-LUMO transitions are represented in blue (solid black line with blue contour) when they occur between levels localized on pair 1-2, and in red (solid black line with red contour), when they occur between levels localized on pair 3-4 (see Fig. 2). Mixed transitions are indicated by dashed lines with blue or red contour. The relative percentages of each transition over the whole trajectory are reported at the bottom of the graph. These transitions have been calculated at the B3LYP level of theory (see method for the definition of the configurations chosen here).

Finally we note that the vibronic contribution to non-radiative recombination processes are expected to be less favorable in the solid than in the molecule, due to a smaller reorganization energy in the solid than in the molecule, which can be estimated from the difference between ΔE^A_{ST} and ΔE^V_{ST}, and due to a broader distribution of f_{OS} over MD trajectories found in the case of the molecule relative to that of the solid (compare Fig. 7c&d with Fig. 10a&b).

Estimate of the ISC and *r*SC Rates

As a final step in understanding the efficiency of the TADF process, we estimated the intersystem (ISC) and reverse intersystem crossing (*r*ISC) rates. As mentioned in the introduction, ISC (a downwards process) occurs (driven by spin-orbit coupling and facilitated by vibronic effects) at all temperature (phosphorescence is indeed measured also at very low T), *r*ISC instead is a spin-forbidden upward process that occurs again thanks to spin-orbit plus vibronic coupling but is only possible if thermal energy is compatible with the singlet-triplet gap. We chose three representative configurations, namely: a) the optimized structure of the molecule at T=0 K; b) one representative molecular snapshot from our FPMD trajectories in the gas phase limit; and c) a molecule which displays the highest f_{OS} extracted as a snapshot of our FPMD simulations conducted in the high packing limit (see Method section for the computational details and Supplementary Table S1 for a summary of data – Supplementary Section S7). The goal of this

analysis is to understand the impact of the *geometry* of the system on the rates, and not to compare in detail with experiment[15, 73] where the NAI-DMAC molecules are embedded into the host matrix (mCPCN). The computed ISC (k_{ISC}) and rISC (k_{rISC}) rates were obtained by assuming an almost complete harvesting of the triplet excitons (see Ref. 15 for details). The k_{ISC} rates are 2.93×10^6 s^{-1}, 4.70×10^5 s^{-1} and 5.80×10^6 s^{-1} for the a), b) and c) models, respectively, while the k_{rISC} rates are 5.63×10^5 s^{-1}, 1.43×10^5 s^{-1} and 8.32×10^4 s^{-1} for the a), b) and c) models, respectively. Our results show that model c), extracted from trajectories obtained for the solid (high-packing fraction limit), exhibits a rISC/ISC ratio (0.01) of the same order of magnitude as that obtained from the available experimental data ($k_{ISC}^{Exp.} = 2.50 \times 10^7$ s^{-1}, $k_{rISC}^{Exp.} = 4.50 \times 10^5$ s^{-1} with (rISC/ISC = 0.02). Instead, models a) and b), representing gas-phase configurations, present similar rate ratios (rISC/ISC = 0.20 and 0.30, respectively), which are one order of magnitude larger than the experimental ones. Although firm conclusions on rates would require averaging over multiple configurations obtained from MD trajectories, the results presented here give a qualitative picture of the difference in rates between gas phase and condensed phase configurations, confirming our findings on the importance of packing.

CONCLUSIONS

Using first principles simulations at finite temperature, coupled with a quantum thermostat, we investigated the structural and electronic properties of a prototypical TADF compound, NAI-DMAC. We studied vertical and adiabatic processes as a function of temperature for the molecule and the crystal. Here the molecule is representative of the gas phase limit and the solid of a high fraction packing limit. We find that increasing the temperature from 0 K to 300 K weakly affects the average value of the adiabatic ΔE_{ST} of the molecule. However, increasing the temperature has a desirable and more sizeable effect on the oscillator

strength that increases by a factor of ~ 3 in the molecule. Packing has a beneficial effect on the ΔE_{ST}, which

is close to zero in the solid also at 300 K, also in the presence of finite temperature fluctuations. Compared

to the molecule, in the solid we find only a more moderate increase in the oscillator strength as a function

of temperature, due to the presence of inter-molecular transitions with low oscillator strength. However,

the reorganization energy is smaller in the solid than in the molecule, pointing at a more pronounced effect

of non-radiative recombination processes in the molecules than in the solid, thus confirming once more the

importance of packing and the desired effect of rigid configurations in condensed phases relative to the gas

phase molecule. We note that the adiabatic value for ΔE_{ST} computed for the molecule (~ 0.3 eV) is an upper

limit to the value measured experimentally, reported to be between 0.04 and 0.09 eV, depending on the

matrix where NAI-DMAC is embedded. Indeed, in the crystal (*i.e.*, for the highest packing), ΔE_{ST} vanishes.

Interestingly the onset of adiabatic values at 300 K is below 0.2 eV in the molecule, namely quite a bit

lower than the average value. Our estimates of the ratio of direct and reverse inter-system crossing rates

point again at the importance of optimizing packing, since the *r*ISC/ISC ratio varies substantially for

configurations in the gas phase and in the crystal. Our theoretical predictions of rate ratios in condensed

phases are consistent with experiments, unlike those obtained for the gas phase, although we cannot yet

draw robust quantitative since we could not average over multiple MD trajectories. Overall, our results

indicate that packing should be designed to have periodic conformations similar those in the crystal, so as

to minimize ΔE_{ST} but with a spacing between molecules large enough so as to avoid the occurrence of inter-

molecular transitions. To achieve such a delicate balance, one might attempt to 'protect' the NAI-DMAC

core by adding steric ligands or π-bridges. In the first case, the substitution of the terminal methyl groups

with, *e.g.,* toluene, naphthalene or carbazole units in the head and tail of the molecule may separate the

emitter molecules while maintaining the desired van der Waals interactions required for packing, consistent

with the suggestions of Park et al.[74] and Chen et al. [75], and recently discussed by Penfold[76]. Alternatively,

by adding π-bridges (*e.g.*, phenylene) a new design of NAI-DMAC derivates may be obtained, with a D-π-A-π-D 'butterfly' concept[8], where the enlargement of the structure may induce a more stable conformation while keeping the solid state system in place.

Our results also indicate that an optimization of the overall geometrical conformation of the molecule is important. We find that the value of the torsion angle between the donor and acceptor moieties is a necessary but not sufficient structural descriptor to predict the values of ΔE_{ST}. Indeed, our simulations show rather different values of the singlet-triplet splitting for the same dihedral angle, depending on the overall configuration, both in classical and quantum trajectories.

Finally, our results points at the importance of including nuclear quantum effects in the simulations of all organic TADF compounds, which we could efficiently consider in our calculations by coupling first principles molecular dynamics with a quantum thermostat. Work is in progress to apply the protocol developed in this work to other TADF compounds and to complex molecular arrangements.

COMPUTATIONAL METHODS

QUANTUM SIMULATIONS AND ELECTRONIC STRUCTURE CALCULATIONS

We carried out first principles molecular dynamics (MD) and electronic structure calculations with the plane wave pseudopotential code Qbox[72] for a) single point calculations, b) geometry optimizations, both in the ground and excited states via ΔSCF-DFT[77, 78], and c) FPMD simulations. Nuclear quantum effects were included by coupling Qbox in client-server mode with iPI (d), adopting the scheme recently described in Kundu et al.[68], where the iPI code[79] updates the nuclear coordinates and the Qbox code supplies forces acting on the nuclei computed within Density Functional Theory (DFT) to iPI. The PBE[69, 70] exchange-correlation functional was used for all calculations, while the B3LYP[33, 34, 35] exchange-correlation functional

was employed in a) and on the geometries obtained in b), c), and d). The SCAN[80, 81, 82] exchange-correlation functional was also employed to carry out FPMD simulations to validate the accuracy of PBE trajectories, with agreement of results not only for structural data but also for vibrational spectra (these will be discussed in detail in a forthcoming publications). In all the cases, the Optimized Norm-Conserving Vanderbilt (ONCV)[83, 84] pseudopotentials were used with a kinetic energy cutoff of 60 Ry, together with a Γ-point sampling of the Brillouin zone of the solid and the Preconditioned Steepest Descent with Anderson (PSDA)[85] acceleration for the wavefunction optimization. The geometry optimizations were considered converged at PBE level when the forces acting on the atoms were found below 10^{-4} Hartree/Bohr for the gas phase system and 10^{-3} Hartree/Bohr for the high packing fraction case, respectively. FPMD and QTMD simulations, both in gas phase and high packing fraction limits, were performed using the Born-Oppenheimer algorithm propagation scheme, with a timestep set to 20 a.u. ($\sim$ 0.5 fs). In FPMD simulations, we used the Bussi-Donadio-Parrinello[86] (BDP) stochastic thermostat, while for the QTMD simulations we used a colored noise Langevin equation. The equilibration runs were performed for $\simeq$ 3 ps for FPMD and 2.5 ps for QTMD for both the molecule and solids, with a subsequent production run of 10 ps.

The D-A nature of the system, which mainly involves transitions between localized HOMO and LUMO levels, offers the possibility to exploit the advantageous ΔSCF-DFT computational method to study and predict the excited state electronic structures of S_1 and T_1 levels, as well as to optimize their geometries, instead of the TD-DFT method, which is more expensive and may, in some cases, pose problems in describing charge-transfer states[87, 88] and excitations in large π-conjugated molecules[89, 90, 91], depending on the functional used. Note however that ΔSCF-DFT can only be used to study low-lying excited states energies involving HOMO-1 $\rightarrow$ LUMO, HOMO $\rightarrow$ LUMO and HOMO $\rightarrow$ LUMO+1 transitions and not the full excitation spectrum, which is instead available to TDDFT calculations. Specifically, the method relies on the possibility of promoting 1 e from, for example, the HOMO to the LUMO level (along spin

channel #1 for S_1 and spin channel #2 for T_1), and to self-consistently optimize the resulting configuration. In particular, in the gas phase limit we investigated the HOMO $\rightarrow$ LUMO transition by choosing an integer occupation of the electronic levels, thus setting occupation for the HOMO = 0 and occupation for the LUMO = 1. The more challenging high packing fraction limit with degenerate single particle states required a more careful choice of electronic occupations. We chose a fractional occupation of $0.75e^-$ x 4 for the HOMO levels (thus creating 1 h^+) and $0.25e^-$ x 4 in the LUMO levels (thus promoting $1e^-$). These occupations have been used both for the single point and geometry optimizations to estimate the ΔE_{ST} energy splitting in absorption and emission.

SAMPLING PROTOCOL

The post-processing analysis of our trajectories involved: 1) the validation of the "accuracy" of the trajectories (see Supplementary Figure S1-S5) as well as 2) an estimate of the autocorrelation function of the dihedral angle to extract non-correlated frames for a meaningful statistical evaluation of the ΔE_{ST} and f_{OS}-value parameters. By using an exponential decay function (*i.e.*, f(x)=exp(-x/τ)), in the gas phase limit trajectory we found a decay time of $\tau = 43.7 \pm 2.2$ fs (corresponding to $\simeq 90$ configurations); thus, we sampled frames every 100 FPMD steps, resulting in a total number of structures equal to 50. However, the complexity of the solid-state system requires a more careful inspection. The computational model representative of the high packing fraction limit is the experimental triclinic unit cell ($P\bar{1}$) structure as deposited by Zeng et al.[15] in the Cambridge Structural Database[92] (CSD Identifier: TESJEJ – 1450555). The structure comprises four molecular units, with the asymmetric unit featuring two molecules with a mutually opposite head-tail orientation (see Fig. 2b). The blue pair molecules in Figure 2b (conf. 1-2), display a torsion angle very close to the gas phase molecule ($\theta \sim 84°$); the red pair molecules (conf. 3-4)

present instead a highly distorted arrangement induced by steric hindrance ($\theta \sim 97°$). The selection of the structures was performed, like for the gas phase limit case, by estimating the decay time (τ) of the dihedral angle autocorrelation functions of the asymmetric unit, where $\tau_{\#1} = 65.0 \pm 1.0$ fs ($\simeq 134$ configurations) and $\tau_{\#3} = 51.0 \pm 1.0$ fs ($\simeq 105$ configurations). To ensure a complete set of uncorrelated configurations, we decided to sample 1 configuration every 250 FPMD steps, obtaining a total number of 84 uncorrelated configurations (see Fig.9).

ISC AND rISC RATES

The ISC and rISC rates between the S_1 and T_1 optimized excited state geometries obtained from the ΔSCF-DFT method, have been computed at T=300 K with the ESD[93, 94] module as implemented in the Orca[95, 96] code (v. 4.2.1), at the B3LYP level of theory, using the Def2-SVP[97] basis set, with the RIJCOSX[98] approximation to accelerate the DFT calculation. The spin-orbit coupling integrals were calculated by means of the RI-SOMF(1X) approximation[99]. The excited states at TDDFT level were computed by means of the TDA approximation[100]. The final rates between the S_1 state and the T_1 sublevels (T_1^1, T_1^0, T_1^{-1}) were calculated as $<k> = (k[S_1\text{-}T_1^1] + k[S_1\text{-}T_1^0] + k[S_1\text{-}T_1^{-1}])/3$ for both ISC and rISC. (See Supplementary Information for details).

2

AUTHOR CONTRIBUTIONS

T. Francese and A. Kundu performed the calculations. T.Francese, F. Gygi and G. Galli designed the research. All authors contributed to the analysis and discussion of the data and the writing of the paper.

NOTES

The authors declare no competing interests.

REFERENCES

1. G. Hong, X. Gan, C. Leonhardt, Z. Zhang, J. Seibert, J. M. Busch and S. Bräse, *Advanced Materials*, 2021, **33**, 2005630.

2. H. Uoyama, K. Goushi, K. Shizu, H. Nomura and C. Adachi, *Nature*, 2012, **492**, 234-238.

3. F. B. Dias, T. J. Penfold and A. P. Monkman, *Methods and applications in fluorescence*, 2017, **5**, 012001.

4. T.-L. Wu, M.-J. Huang, C.-C. Lin, P.-Y. Huang, T.-Y. Chou, R.-W. Chen-Cheng, H.-W. Lin, R.-S. Liu and C.-H. Cheng, *Nature Photonics*, 2018, **12**, 235-240.

5. T.-A. Lin, T. Chatterjee, W.-L. Tsai, W.-K. Lee, M.-J. Wu, M. Jiao, K.-C. Pan, C.-L. Yi, C.-L. Chung, K.-T. Wong and C.-C. Wu, *Advanced Materials*, 2016, **28**, 6976-6983.

6. H. Yersin, *Highly efficient OLEDs: Materials based on thermally activated delayed fluorescence* . John Wiley & Sons, 2019.

7. J. Lee, K. Shizu, H. Tanaka, H. Nomura, T. Yasuda and C. Adachi, *Journal of Materials Chemistry C*, 2013, **1**, 4599.

8. S. Y. Lee, T. Yasuda, Y. S. Yang, Q. Zhang and C. Adachi, *Angewandte Chemie International Edition*, 2014, **53**, 6402-6406.

9. Q. Zhang, H. Kuwabara, W. J. Potscavage, S. Huang, Y. Hatae, T. Shibata and C. Adachi, *Journal of the American Chemical Society*, 2014, **136**, 18070-18081.

10. S. Wang, X. Yan, Z. Cheng, H. Zhang, Y. Liu and Y. Wang, *Angewandte Chemie International Edition*, 2015, **54**, 13068-13072.

11. J.-X. Chen, K. Wang, C.-J. Zheng, M. Zhang, Y.-Z. Shi, S.-L. Tao, H. Lin, W. Liu, W.-W. Tao, X.-M. Ou and X.-H. Zhang, *Advanced Science*, 2018, **5**, 1800436.

12. J.-X. Chen, W.-W. Tao, Y.-F. Xiao, K. Wang, M. Zhang, X.-C. Fan, W.-C. Chen, J. Yu, S. Li, F.-X. Geng, X.-H. Zhang and C.-S. Lee, *ACS Applied Materials & Interfaces*, 2019, **11**, 29086-29093.

13. X.-C. Fan, K. Wang, C.-J. Zheng, G.-L. Dai, Y.-Z. Shi, Y.-Q. Li, J. Yu, X.-M. Ou and X.-H. Zhang, *Journal of Materials Chemistry C*, 2019, **7**, 8923-8928.

14. M. Y. Wong and E. Zysman-Colman, *Advanced Materials*, 2017, **29**, 1605444.

15. W. Zeng, H.-Y. Lai, W.-K. Lee, M. Jiao, Y.-J. Shiu, C. Zhong, S. Gong, T. Zhou, G. Xie, M. Sarma, K.-T. Wong, C.-C. Wu and C. Yang, *Advanced Materials*, 2018, **30**, 1704961.

16. T. Chen, C.-H. Lu, C.-W. Huang, X. Zeng, J. Gao, Z. Chen, Y. Xiang, W. Zeng, Z. Huang, S. Gong, C.-C. Wu and C. Yang, *Journal of Materials Chemistry C*, 2019, **7**, 9087-9094.

17. F.-M. Xie, H.-Z. Li, G.-L. Dai, Y.-Q. Li, T. Cheng, M. Xie, J.-X. Tang and X. Zhao, *ACS Applied Materials & Interfaces*, 2019, **11**, 26144-26151.

18. X. Song, D. Zhang, T. Huang, M. Cai and L. Duan, *Science China Chemistry*, 2018, **61**, 836–843.

19. J. H. Kim, J. H. Yun and J. Y. Lee, *Advanced Optical Materials*, 2018, **6**, 1800255.

20. J. Li, T. Nakagawa, J. Macdonald, Q. Zhang, H. Nomura, H. Miyazaki and C. Adachi, *Advanced Materials*, 2013, **25**, 3319-3323.

21. C. J. Christopherson, D. M. Mayder, J. Poisson, N. R. Paisley, C. M. Tonge and Z. M. Hudson, *ACS Applied Materials & Interfaces*, 2020, **12**, 20000-20011.

22. M. Jakoby, S. Heidrich, L. Graf Von Reventlow, C. Degitz, S. M. Suresh, E. Zysman-Colman, W. Wenzel, B. S. Richards and I. A. Howard, *Chemical Science*, 2021, **12**, 1121-1125.

23. L. B. McGown and K. Nithipatikom, *Applied Spectroscopy Reviews*, 2000, **35**, 353-393.

24. M.-S. Lin, S.-J. Yang, H.-W. Chang, Y.-H. Huang, Y.-T. Tsai, C.-C. Wu, S.-H. Chou, E. Mondal and K.-T. Wong, *Journal of Materials Chemistry*, 2012, **22**, 16114.

25. E. Runge and E. K. U. Gross, *Physical Review Letters*, 1984, **52**, 997-1000.

26. E. K. U. Gross, J. F. Dobson and M. Petersilka, in *Density Functional Theory II: Relativistic and Time Dependent Extensions*, ed. R. F. Nalewajski, Springer Berlin Heidelberg, Berlin, Heidelberg, 1996, DOI: 10.1007/BFb0016643, pp. 81-172.

27. A. Warshel and M. Levitt, *Journal of Molecular Biology*, 1976, **103**, 227-249.

28. L. Lv, K. Liu, K. Yuan, Y. Zhu and Y. Wang, *RSC Advances*, 2018, **8**, 28421-28432.

29. S. Miertuš, E. Scrocco and J. Tomasi, *Chemical Physics*, 1981, **55**, 117-129.

30. S. Miertuš and J. Tomasi, *Chemical Physics*, 1982, **65**, 239-245.

31. J.-M. Mewes, *Physical Chemistry Chemical Physics*, 2018, **20**, 12454-12469.

32. T. Hu, G. Han, Z. Tu, R. Duan and Y. Yi, *The Journal of Physical Chemistry C*, 2018, **122**, 27191-27197.

33. A. D. Becke, *The Journal of Chemical Physics*, 1993, **98**, 5648-5652.

34. K. Kim and K. D. Jordan, *The Journal of Physical Chemistry*, 1994, **98**, 10089-10094.

35. P. J. Stephens, F. J. Devlin, C. F. Chabalowski and M. J. Frisch, *The Journal of Physical Chemistry*, 1994, **98**, 11623-11627.

36. P. K. Samanta, D. Kim, V. Coropceanu and J.-L. Brédas, *Journal of the American Chemical Society*, 2017, **139**, 4042-4051.

37. K. Zhang, L. Cai, J. Fan, Y. Zhang, L. Lin and C.-K. Wang, *Spectrochimica Acta Part A: Molecular and Biomolecular Spectroscopy*, 2019, **209**, 248-255.

38. J. Fan, Y. Zhang, Y. Ma, Y. Song, L. Lin, Y. Xu and C.-K. Wang, *Journal of Materials Chemistry C*, 2020, **8**, 8601-8612.

39. J. Liu, J. Fan, K. Zhang, Y. Zhang, C.-K. Wang and L. Lin, *Chinese Physics B*, 2020, **29**, 088504.

40. H. Sun, Z. Hu, C. Zhong, X. Chen, Z. Sun and J.-L. Brédas, *The Journal of Physical Chemistry Letters*, 2017, **8**, 2393-2398.

41. Y. Zhang, Y. Ma, K. Zhang, Y. Song, L. Lin, C.-K. Wang and J. Fan, *Spectrochimica Acta Part A: Molecular and Biomolecular Spectroscopy*, 2020, **241**, 118634.

42. J. Fan, Y. Zhang, Y. Zhou, L. Lin and C.-K. Wang, *The Journal of Physical Chemistry C*, 2018, **122**, 2358-2366.

43. Y. Ma, K. Zhang, Y. Zhang, Y. Song, L. Lin, C.-K. Wang and J. Fan, *Molecular Physics*, 2021, **119**, e1862931.

44. Q. Lu, G. Jiang, F. Li, L. Lin, C.-K. Wang, J. Fan and Y. Song, *Spectrochimica Acta Part A: Molecular and Biomolecular Spectroscopy*, 2020, **229**, 117964.

45. R. Dhali, D. K. A. Phan Huu, F. Terenziani, C. Sissa and A. Painelli, *The Journal of Chemical Physics*, 2021, **154**, 134112.

46. J. S. Clawson, K. L. Anderson, R. J. Pugmire and D. A. Grant, *Journal of Physical Chemistry A*, 2004, **108**, 2638-2644.

47. X. M. Gan, X. Y. Wu, R. M. Yu and C. Z. Lu, *Chinese Journal of Structural Chemistry*, 2018, **37**, 1749-1755.

48. R. Giereth, A. K. Mengele, W. Frey, M. Kloss, A. Steffen, M. Karnahl and S. Tschierlei, *Chemistry-a European Journal*, 2020, **26**, 2675-2684.

49. S. Keller, M. Bantle, A. Prescimone, E. C. Constable and C. E. Housecroft, *Molecules*, 2019, **24**.

50. D. Liang, J. H. Jia, J. Z. Liao, R. M. Yu and C. Z. Lu, *Chinese Journal of Structural Chemistry*, 2017, **36**, 82-88.

51. L. Lin, X. L. Chen, D. H. Chen, X. Y. Wu, R. M. Yu and C. Z. Lu, *Chinese Journal of Structural Chemistry*, 2017, **36**, 1493-1501.

52. H. Mubarok, W. Lee, T. Lee, J. Jung, S. Yoo and M. H. Lee, *Frontiers in Chemistry*, 2020, **8**.

53. M. Osawa, M. Hashimoto, I. Kawata and M. Hoshino, *Dalton Transactions*, 2017, **46**, 12446-12455.

54. J. S. Ward, R. S. Nobuyasu, M. A. Fox, J. A. Aguilar, D. Hall, A. S. Batsanov, Z. J. Ren, F. B. Dias and M. R. Bryce, *Journal of Organic Chemistry*, 2019, **84**, 3801-3816.

55. H. X. Xu, Y. P. Zhao, J. Zhang, D. Zhang, Y. Q. Miao, J. Shinar, R. Shinar, H. Wang and B. S. Xu, *Organic Electronics*, 2019, **74**, 13-22.

56. W. W. Zhao, X. X. Shang, R. M. Yu and C. Z. Lu, *Chinese Journal of Structural Chemistry*, 2017, **36**, 1368-1374.

57. D. Zhou, C. H. Ryoo, D. H. Liu, S. Y. Wang, G. W. Qian, Y. Q. Zheng, S. Y. Park, W. G. Zhu and Y. F. Wang, *Advanced Optical Materials*, 2020, **8**.

58. A. Pershin, D. Hall, V. Lemaur, J.-C. Sancho-Garcia, L. Muccioli, E. Zysman-Colman, D. Beljonne and Y. Olivier, *Nature Communications*, 2019, **10**.

59. D. Sun, S. M. Suresh, D. Hall, M. Zhang, C. Si, D. B. Cordes, A. M. Z. Slawin, Y. Olivier, X. Zhang and E. Zysman-Colman, *Materials Chemistry Frontiers*, 2020, **4**, 2018-2022.

60. S. A. Servan, A. Ünal, B. Hamarat and U. Bozkaya, *The Journal of Physical Chemistry A*, 2020, **124**, 6889-6898.

61. Y. Wada, K. Shizu and H. Kaji, *The Journal of Physical Chemistry A*, 2021, **125**, 4534-4539.

62. S. W. Park, J. H. Yang, H. Choi, Y. M. Rhee and D. Kim, *The Journal of Physical Chemistry A*, 2020, **124**, 10384-10392.

63. M. Ceriotti, G. Bussi and M. Parrinello, *Physical review letters*, 2009, **103**, 030603.

64. G. Tu, Q. Zhou, Y. Cheng, Y. Geng, L. Wang, D. Ma, X. Jing and F. Wang, *Synthetic Metals*, 2005, **152**, 161-164.

65. A. Demeter, T. Bérces, L. Biczók, V. Wintgens, P. Valat and J. Kossanyi, *The Journal of Physical Chemistry*, 1996, **100**, 2001-2011.

66. D. Kolosov, V. Adamovich, P. Djurovich, M. E. Thompson and C. Adachi, *Journal of the American Chemical Society*, 2002, **124**, 9945-9954.

67. Q. Zhang, B. Li, S. Huang, H. Nomura, H. Tanaka and C. Adachi, *Nature Photonics*, 2014, **8**, 326-332.

68. A. Kundu, M. Govoni, H. Yang, M. Ceriotti, F. Gygi and G. Galli, *Physical Review Materials*, 2021, **5**.

69. J. P. Perdew, K. Burke and M. Ernzerhof, *Physical Review Letters*, 1996, **77**, 3865-3868.

70. J. P. Perdew, K. Burke and M. Ernzerhof, *Physical Review Letters*, 1997, **78**, 1396-1396.

71. R. Resta, *Physical Review Letters*, 1998, **80**, 1800-1803.

72. F. Gygi, *IBM Journal of Research and Development*, 2008, **52**, 137-144.

73. T. Chen, C.-H. Lu, C.-W. Huang, X. Zeng, J. Gao, Z. Chen, Y. Xiang, W. Zeng, Z. Huang and S. Gong, *Journal of Materials Chemistry C*, 2019, **7**, 9087-9094.

74. I. S. Park, J. Lee and T. Yasuda, *Journal of Materials Chemistry C*, 2016, **4**, 7911-7916.

75. X.-K. Chen, B. W. Bakr, M. Auffray, Y. Tsuchiya, C. D. Sherrill, C. Adachi and J.-L. Bredas, *The journal of physical chemistry letters*, 2019, **10**, 3260-3268.

76. J. Eng and T. J. Penfold, *Communications Chemistry*, 2021, **4**, 1-4.

77. H. R. Zhekova, M. Seth and T. Ziegler, *International Journal of Quantum Chemistry*, 2014, **114**, 1019-1029.

78.   T. Kowalczyk, S. R. Yost and T. V. Voorhis, *The Journal of Chemical Physics*, 2011, **134**, 054128.

79.   V. Kapil, M. Rossi, O. Marsalek, R. Petraglia, Y. Litman, T. Spura, B. Cheng, A. Cuzzocrea, R. H. Meißner and D. M. Wilkins, *Computer Physics Communications*, 2019, **236**, 214-223.

80.   J. Sun, A. Ruzsinszky and J. P. Perdew, *Physical Review Letters*, 2015, **115**.

81.   R. Car, *Nature Chemistry*, 2016, **8**, 820-821.

82.   M. D. Lacount and F. Gygi, *The Journal of Chemical Physics*, 2019, **151**, 164101.

83.   D. R. Hamann, *Physical Review B*, 2013, **88**.

84.   M. Schlipf and F. Gygi, *Computer Physics Communications*, 2015, **196**, 36-44.

85.   D. G. Anderson, *Journal of the ACM*, 1965, **12**, 547-560.

86.   G. Bussi, D. Donadio and M. Parrinello, *The Journal of Chemical Physics*, 2007, **126**, 014101.

87.   A. Dreuw and M. Head-Gordon, *Journal of the American Chemical Society*, 2004, **126**, 4007-4016.

88.   M. J. G. Peach, P. Benfield, T. Helgaker and D. J. Tozer, *The Journal of Chemical Physics*, 2008, **128**, 044118.

89.   S. Grimme and M. Parac, *ChemPhysChem*, 2003, **4**, 292-295.

90.   M. Wanko, M. Garavelli, F. Bernardi, T. A. Niehaus, T. Frauenheim and M. Elstner, *The Journal of Chemical Physics*, 2004, **120**, 1674-1692.

91.   Z.-L. Cai, K. Sendt and J. R. Reimers, *The Journal of Chemical Physics*, 2002, **117**, 5543-5549.

92.   C. R. Groom, I. J. Bruno, M. P. Lightfoot and S. C. Ward, *Acta Crystallographica Section B Structural Science, Crystal Engineering and Materials*, 2016, **72**, 171-179.

93.   B. De Souza, F. Neese and R. Izsák, *The Journal of Chemical Physics*, 2018, **148**, 034104.

94.   B. De Souza, G. Farias, F. Neese and R. Izsák, *Journal of Chemical Theory and Computation*, 2019, **15**, 1896-1904.

95.   F. Neese, *Wiley Interdisciplinary Reviews: Computational Molecular Science*, 2012, **2**, 73-78.

96.   F. Neese, *WIREs Computational Molecular Science*, 2018, **8**, e1327.

97.   F. Weigend and R. Ahlrichs, *Physical Chemistry Chemical Physics*, 2005, **7**, 3297.

98.   F. Neese, F. Wennmohs, A. Hansen and U. Becker, *Chemical Physics*, 2009, **356**, 98-109.

99.   F. Neese, *The Journal of Chemical Physics*, 2005, **122**, 034107.

100.   T. Petrenko, S. Kossmann and F. Neese, *The Journal of Chemical Physics*, 2011, **134**, 054116.